Deionization shock waves and ionic separations in heterogeneous porous media

Alexander D. Sapp⬤

Bioseparation Engineering Group, TUM School of Engineering and Design,
Technical University of Munich, 85748 Garching, Germany

Huanhuan Tian and Martin Z. Bazant⬤[*]

Department of Chemical Engineering, Massachusetts Institute of Technology,
Cambridge, Massachusetts 02139, USA

The electrochemical separation of charged species is becoming increasingly relevant for industry. A developing set of promising technologies in this space centers around the utilization of deionization shocks in porous, charged materials. To date, primarily homogeneous media have been investigated; however, heterogeneities are present in many porous structures and have been hypothesized to improve performance. Throughout this study, we demonstrate that heterogeneity in the porous structure area density and surface charge density of a crossflow shock electrodialysis cell leads to substantial vortex formation in the depletion zone. Vortices are dependent on the extent of alternating high and low permeabilities, in addition to the expanse of the depletion zone, greatly affecting performance. Heterogeneities in the geometry of the media may lead to an increased selectivity at lower energy input and also exert a strong influence when hierarchical structures are present.

I. INTRODUCTION

Efforts surrounding the separation of ions from aqueous solutions have traditionally centered around producing water of high purity, e.g., converting brines through desalination and decontamination to hygienic drinking water or generating water with effectively no trace components for pharmaceutical or microelectronic applications [1,2]. Commonly, thermal or pressure-driven membrane technologies have been utilized in this context—notably distillation and reverse osmosis (RO). However, electrochemical methods have been recently generating increased attention [3].

Similar to RO, electrochemical unit operations exhibit a reduced dependability on fossil fuels in comparison to thermal separation, as they solely rely on electrical power and are easily integrable into an industrial landscape centered around renewables [4–7]. Though shortcomings have been pointed out in terms of energy efficiency for classic (seawater) desalination, in cases of many consecutive steps or for difficult separation problems of highly dilute solutions, electrochemical methods are better suited, e.g., through their superior scaling [8–11]. Additionally, this makes them very attractive for isolating high value species from solutions, such as rare metals or biological compounds, the latter of which are very sensitive to harsh physical conditions.

The foundation for many advanced electrochemical methods is electrodialysis (ED). ED offers similar advantages to RO but overall its industrial applications are limited [3,12,13]. Efficiency

---

[*]Contact author: bazant@mit.edu

issues caused by concentration polarization [14,15], nontrivial selectivity for both membrane types [16–18], and fouling [19,20] represent drawbacks of basic ED setups.

Maintaining most advantages of ED, a promising alternative called shock electrodialysis (SED) has materialized over the last decade [21]. SED improves upon ED by achieving currents beyond the diffusion limit [22], eliminating fouling through the possibility of membraneless implementations [23–25], and has recently proven reliable in terms of selectivity [26], pointing towards its applicability as a separation or purification unit operation.

SED is an electrokinetically driven technique in which a brine, flowing through a slightly charged, porous structure, is subjected to a depletion zone with a sharp border that propagates in a shocklike fashion at overlimiting current (OLC) [24,27]. Contrary to other mechanisms of OLC, such as current-induced membrane discharge [28], water dissociation [29,30], or Taylor-Aris dispersion [31,32], the effects of SED stem from surface conduction and/or electro-osmotic flow (EOF)—a result of the microchannels, usually in the order of $0.1-1$ μm that constitute the porous media [23,33].

Following research on micro-nanochannel junctions by Mani, Zangle, and Santiago at Stanford [34,35], Bazant and co-workers laid the groundwork for an SED process, formulating a general macroscopic continuum model—the basis for simulation studies to date [21,22,36]. Further research into deionization shocks in nanopores was conducted by Yaroshchuk [37]. Shortly after, Dydek and Bazant [33] concluded with an analysis of an initial two-dimensional (2D) crossflow configuration, thereby, providing the foundation for modeling and experimental research [23]. The first continuous and scalable design for SED was reported by Schlumpberger *et al.* [24], with a major secondary discovery that high water recovery was achievable, related to electro-osmotic pumping. Continuing experimental work demonstrated the possibility of selective separation of ions in mixtures, including classic model electrolytes [27], radionuclides [25], or lead in competition with sodium [26].

Simultaneously, efforts in modeling were intensified. Schlumpberger *et al.* [38] effectively used the Nernst-Planck equation to simulate a 2D SED device for binary electrolyte desalination, revisiting the group's earlier experimental work [24]. The simulation was able to predict an increased water recovery but overestimated the desalination at a given applied current. Tian *et al.* [39] expanded upon previous theoretical work, achieving closer alignment to experimental results and capturing selectivity differences [26]. The model was developed by depth averaging a Poisson-Nernst-Planck description of planar channels, while additionally including water dissociation. This being said, to date primarily homogeneous material properties have been the focus of simulation studies with only a few exceptions.

Alizadeh *et al.* [40] investigated the effects of hierarchical as well as nonhierarchical random porous networks for a similar system as used by Deng *et al.* [23]. Pores of different sizes were explicitly captured using the group's porous electrokinetic computational framework [41,42]. However, no crossflow was imposed and the porous material was enclosed only on one side by a membrane.

Focusing on the flow in charged porous structures without an external electric field, Mirzadeh *et al.* [43] recently analyzed electrokinetic phenomena in heterogeneous porous media. Contrary to Alizadeh *et al.* [40], they used effective permeabilities in a continuum framework instead of modeling individual channels. Their results demonstrate the development of complex flow and increased mixing in charged porous media solely based on heterogeneous hydrodynamic permeabilities.

Experimentally, Alkhadra *et al.* [44] utilized concentration shocks for heavy metal ion extraction, where the porous material was substituted with an ion exchange resin wafer (IERW) [45,46]. An IERW consisted of cation exchange resin beads immobilized in a macroporous binder, constituting a hierarchical structure. The process, which resembles ion exchange (IEX) rather than ED, demonstrated the versatile use of concentration shocks.

This most current body of research highlights the importance of heterogeneous material properties, a thorough understanding of which could guide material design, add in selective separation, while additionally representing real-world porous materials more closely.

Consequently, we introduce heterogeneity using the methodology of Mirzadeh *et al.* [43] and apply it to the modeling framework of Schlumpberger *et al.* [38], to understand the impact on SED

performance as well as selectivity. Furthermore, we take a first step towards modeling hierarchical properties and understanding their effects in the context of deionization shocks. Our aim is to highlight the trade-offs that can stem from heterogeneous materials for electrokinetic applications. We hope to inspire further experimental and simulation work that employ engineered nonhomogeneous materials and concentration shocks to solve challenges surrounding selective separation, removal of trace components, as well as classic desalination.

II. THEORETICAL DESCRIPTION

Substantial progress on the theory of shock electrodialysis has been made over the recent years [22,33,39,47]. In line with previous work—allowing for considerable simplification without too much loss in applicability—we assume a dilute electrolyte [33,35,38,39]. Our model utilizes the equivalent set of equations reported by Schlumpberger *et al.* [38] and initially proposed by Mani and Bazant [22].

A. Transport equations

To describe the transport in the SED device, the fluxes are expressed through the Nernst-Planck equation (vectors are represented by bold symbols). Taking advantage of the Bruggeman correlation leads to [38,48,49]

$$\boldsymbol{F}_i = \epsilon_p^{1.5}\left(-D_i\boldsymbol{\nabla} c_i + \boldsymbol{u}c_i - \frac{D_i z_i e}{kT}c_i\boldsymbol{\nabla}\phi\right). \tag{1}$$

Herein, D is the effective diffusion coefficient, assumed to be constant for each species i, c the concentration, z the valence, k the Boltzmann constant, T the temperature, ϕ the electrostatic potential, e the elementary charge, ϵ_p the porosity, and $\boldsymbol{u}$ the velocity. Instead of solving the generalized Navier-Stokes equations with an additional electrical term [50], we employ simpler, linear dependencies expressing the convection $\boldsymbol{u}$ by adding to Darcy's law an electro-osmotic flow contribution [22,39]

$$\boldsymbol{u} = -k_{eo}\boldsymbol{\nabla}\phi - k_d\boldsymbol{\nabla}p. \tag{2}$$

p is the pressure and k_d the hydrodynamic permeability:

$$k_d = \frac{h_p^2}{2\mu}, \tag{3}$$

stemming from the original Darcy correlation [51]. Analogously, k_{eo} represents the electro-osmotic permeability defined through the Helmholtz-Smoluchowski [38] expression

$$k_{eo} = -\frac{\epsilon_w\zeta}{\mu}. \tag{4}$$

μ is the electrolyte's viscosity, approximated to be constant, ϵ_w the permittivity of water, ζ the zeta potential of the porous material, and h_p the characteristic pore size:

$$h_p = \frac{\epsilon_p}{a_p}, \tag{5}$$

where a_p is the porous structure area density. Accurately determining the ζ potential and surface charge density in dependence on the electrolyte concentration, pH, or geometry is an ongoing field of research [52–54]. For simplicity and numerical stability, we restrict ourselves to silica materials and adopt an approach where the surface charge density σ_s is set, calculating the ζ potential through [55,56]

$$\zeta = \frac{k_e}{\left[\ln\left(\frac{-\sigma_s}{e\Gamma+\sigma_s}\right) + \ln(10)(\mathrm{p}K_a - \mathrm{pH})\right] - \frac{\sigma_s}{C}} \tag{6}$$

in which Γ is the silanol group density, pK_a the deprotonation constant, and C the Stern layer capacitance.

For a system with N ionic species, $N + 2$ variables need to be solved for—the concentrations c_i, the pressure p, and potential ϕ. For each species a conservation equation of the form

$$\frac{\partial(\epsilon_p c_i)}{\partial t} + \nabla \cdot \mathbf{F}_i = 0 \quad \text{for} \quad i = 1, 2, \ldots, N \tag{7}$$

may be formulated. Additionally, the mass conservation accounting for local porosity variations [22]

$$\nabla \cdot \left(\epsilon_p^{1.5} \mathbf{u}\right) = 0 \tag{8}$$

is utilized. To close the system, electroneutrality is enforced—adding to the classical formulation a term accounting for the volumetric surface charge density ρ_s of the porous material:

$$\sum_i z_i c_i e + \rho_s = 0 \quad \text{with} \quad \rho_s = \frac{\sigma_s}{h_p}. \tag{9}$$

Therefore, the dimensionless (see Table I) set of equations is

$$\frac{\partial(\epsilon_p \tilde{c}_i)}{\partial \tilde{t}} + \tilde{\nabla} \cdot \left[\epsilon_p^{1.5}(-\tilde{D}_i \tilde{\nabla}\tilde{c}_i + \tilde{\mathbf{u}}\tilde{c}_i - z_i \tilde{D}_i \tilde{c}_i \tilde{\nabla}\tilde{\phi})\right] = 0, \tag{10}$$

$$\tilde{\nabla} \cdot \left[\epsilon_p^{1.5}(-\tilde{k}_{eo}\tilde{\nabla}\tilde{\phi} - \tilde{k}_d \tilde{\nabla}\tilde{p})\right] = 0, \tag{11}$$

$$\sum_i z_i \tilde{c}_i + \tilde{\rho}_s = 0. \tag{12}$$

If not otherwise specified, all values, with the exception of the performance metrics (see Sec. III D), are reported in dimensionless form. A tilde is used to designate dimensionless quantities.

B. Heterogeneity

Mirzadeh *et al.* [43] have demonstrated that in charged porous media with a heterogeneous permeability, complex flow patterns—up to vortices—can be observed depending on the ratio between hydrodynamic and electro-osmotic influencing factors. Using their macroscopic approach, which is easily integrated into our existing models, we incorporate a random field expression $z(\mathbf{x})$ for properties $\gamma(\mathbf{x})$, e.g., the surface charge density σ_s, to imitate heterogeneity

$$\gamma(\mathbf{x}) = \gamma_0 \exp[z(\mathbf{x})], \tag{13}$$

γ_0 being the space-independent base value. $z(\mathbf{x})$ is connected to a prescribed, statistically isotropic $[\xi(\mathbf{x}) = \xi(|\mathbf{x}|)]$ autocorrelation function $\xi(\mathbf{x})$ through

$$\xi(\mathbf{x}) = \int z(\mathbf{x}')z(\mathbf{x}' - \mathbf{x})d\mathbf{x}'. \tag{14}$$

As the Wiener-Khinchin theorem relates the autocorrelation function to the spectral density $S(\mathbf{k})$ through a Fourier transform $\mathcal{F}$, an efficient computation of the random field can be obtained by first calculating

$$S(\mathbf{k}) = \mathcal{F}\xi(\mathbf{x}) \quad (= |\mathcal{F}z(\mathbf{x})|^2) \tag{15}$$

and then plugging the result in

$$z(\mathbf{x}) = \mathcal{F}^{-1}\{\sqrt{S(|\mathbf{k}|)} \exp[i\theta(\mathbf{k})]\}, \tag{16}$$

utilizing the fast Fourier transform [43,57,58]. The term $\exp[i\theta(\mathbf{k})]$ introduces randomness as $\theta(\mathbf{k})$, fulfilling $\theta(\mathbf{k}) = \theta(-\mathbf{k})$, and is arbitrarily pooled from $\mathcal{U}(0, 2\pi)$. Applying a Gaussian

TABLE I. Symbols, values, units, and nondimensionalization of simulation parameters.

Description	Parameter	Value	Unit	Nondimensional scale
Anion diffusion coefficient	D_-		$m^2\,s^{-1}$	D_-
Chloride		2.032×10^{-9}		
Sulfate		1.065×10^{-9}		
Applied voltage	V	Varies	V	$\frac{kT}{e}$
Autocorrelation function	ξ	Varies		
Gaussian autocorrelation factor	ξ_0	1		
Boltzmann constant	k	1.381×10^{-23}	$J\,K^{-1}$	
Bulk pH	pH	7.0		
Cation diffusion coefficient	D_+		$m^2\,s^{-1}$	D_-
Sodium		1.334×10^{-9}		
Magnesium		0.706×10^{-9}		
Characteristic pore size	h_p	Varies	m	
Base case		2.689×10^{-7}		
Concentration	c	Varies	m^{-3}	$s_- c_0$
Conductance	κ	Varies	S	κ_{sc}
Correlation length	l	0.1		
Current	I	Varies	A	$z_+ s_+ c_0 e Q_{feed}$
Current efficiency	η	Varies	%	
Darcy (hydrodynamic) permeability	k_d	Varies	$m^2\,Pa^{-1}\,s^{-1}$	$D_- p_{amb}$
Degree of desalination	χ	Varies	%	
Electronic charge	e	1.602×10^{-19}	C	
Electro-osmotic permeability	k_{eo}	Varies	$m^2\,V^{-1}\,s^{-1}$	$\frac{D_- e}{kT}$
Energy consumption	ε	Varies	$kJ\,L^{-1}$	
Flux	$\boldsymbol{F}$	Varies	$m^{-2}\,s^{-1}$	$\frac{D_- s_- c_0}{H}$
Fourier space vector	$\boldsymbol{k}$	Varies	m^{-1}	
Height	H	2.7	mm	H
Height to concentrate outlet	H_{oc}	2.025	mm	H
Height to diluate outlet	H_{od}	0.675	mm	H
Height to inlet	H_i	1.35	mm	H
Inlet/outlet height	H_{io}	0.49	mm	H
Length	L	10	mm	H
Length inlet/outlet	L_{io}	0.548	mm	H
Mean	μ	Varies		
Porosity	ϵ_p	Varies		
Base case		0.48		
Porous structure area density	a_p		m^{-1}	
Base case		1.785×10^6		
Potential	ϕ	Varies	V	$\frac{kT}{e}$
Pressure	p	Varies	Pa	p_{amb}
Random field	z	Varies		
Silanol (de)protonation constant	pK	7.5		
Silanol surface charge density	Γ	8×10^{-18}	m^{-2}	
Space vector	$\boldsymbol{x}$	Varies	m	H
Stern layer capacitance	C	2.9	$F\,m^{-2}$	
Stoichiometric coefficient	s	Varies		
Surface charge density	σ_s	Varies	$mC\,m^{-2}$	
Base case		-20.80		
Temperature	T	298	K	

TABLE I. (*Continued.*)

Description	Parameter	Value	Unit	Nondimensional scale
Valence	z	Varies		
Variance	σ^2	Varies		
Velocity	$\boldsymbol{u}$	Varies	$m\,s^{-1}$	$\frac{D_-}{H}$
Volumetric flow rate	Q	Varies	$m^3\,s^{-1}$	
Volumetric surface charge	ρ_s	Varies	$C\,m^{-3}$	
Water permittivity	ϵ_w	6.947×10^{-10}	$F\,m^{-1}$	
Water recovery	ω	Varies		
Water viscosity	μ	1.002×10^{-3}	$Pa\,s$	
Width	W	20	mm	H
Zeta potential	ζ	Varies	V	

autocorrelation function,

$$\xi(\boldsymbol{x}) = \xi_0 \exp\left(\frac{|\boldsymbol{x}|^2}{l^2}\right) \quad \text{with} \quad \xi_0 = \sigma^2 + \mu^2 \tag{17}$$

as done by Mirzadeh *et al.* [43]. The mean μ and variance σ^2 dictate the Gaussian autocorrelation factor ξ_0 which determines the variance in $z(\boldsymbol{x})$. Additionally, the autocorrelation length l influences the distance between variations in a property—the smaller l the less correlated the random field and the coarser the property distribution. Using this approach leads to a log-normal distribution for the respective property $\gamma(\boldsymbol{x})$ with the degree of correlation determined by $\xi(\boldsymbol{x})$ [43].

III. SIMULATION IMPLEMENTATION

We model an SED setup as displayed in Fig. 1 and initially focus on the binary electrolyte NaCl. Later we also report results for a model electrolyte of $MgCl_2$-$MgSO_4$ to understand selectivity influences. In contrast to some previous studies we have decided to model the inlet and outlets as channels, mimicking possible future implementations. To use the same set of equations throughout our system, the inlet and outlets are assigned zero charge, a unity porosity, and a tenfold larger hydrodynamic permeability. In our setup the wall between the outlets separates the concentrated and diluted streams, analogous to Tian *et al.* [26]. In contrast, Schlumpberger *et al.* [38] used a thin splitter.

As in previous SED studies, our porous materials are based on silica, thereby allowing us to use the aforementioned ζ-potential computation. Since we align our system to the work of Schlumpberger *et al.* [38], we use a base porosity of $\epsilon_p = 0.48$, with a base porous structure area
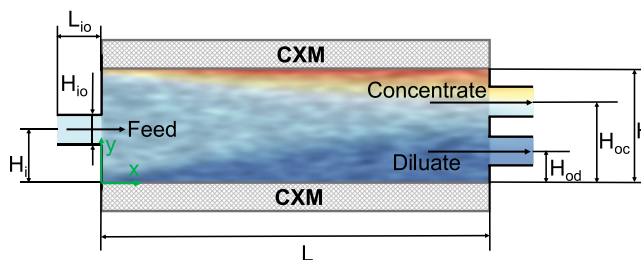

FIG. 1. Sketch of the simulated shock electrodialysis setup. A feed containing a binary electrolyte is separated into a diluate and concentrate stream by passing through a slightly negatively charged porous medium that is sandwiched between two cation exchange membranes (CXMs) with a potential $\phi = \pm\frac{V}{2}$, respectively.

density of $1.785 \times 10^{-6} \, \text{m}^{-1}$ (Brunauer-Emmett-Teller surface area: $a_{\text{frit}} = 1.75 \, \text{m}^2 \, \text{g}^{-1}$; density: $\rho_{\text{frit}} = 1.02 \, \text{g} \, \text{cm}^{-3}$) and base surface charge density depending on the electrolyte. For all simulations, excluding the ones surrounding selectivity, we employ 10-mM NaCl solutions, so that $\sigma_{\text{s}} = -20.80 \, \text{mC} \, \text{m}^{-2}$, whereas a hypothetical value of $-10.42 \, \text{mC} \, \text{m}^{-2}$ is set for the magnesium-chloride-sulfate mixture in the selectivity section. Herein, the inlet concentration is 1 mM for both $MgCl_2$ and $MgSO_4$. Consistently, the volumetric flow rate equals $Q_{\text{feed}} = 76 \, \text{µL} \, \text{min}^{-1}$. Material and geometrical parameters can be found in Table I.

The cation exchange membranes CXMs are assumed to have a uniform potential $\phi = V$ which we vary. Instead of explicitly modeling them, the CXMs are assumed to be ideal, $F_{y,-} = 0$.

To solve our system, we employ a finite-volume approach and report steady-state results. Our mesh for the SED cell, i.e., excluding the inlet and outlets, was 114×48, and the inlet and outlets each 16×8.

A. Boundary conditions

At the inlet a Dirichlet boundary condition for the concentrations $c_{i,\text{feed}}$ is imposed. The velocity $u_{\text{feed}} = \frac{Q_{\text{feed}}}{H_{\text{io}}W}$ is constant and determined by the flow rate Q_{feed}, the inlet/outlet height H_{io}, and device width W. A Neumann boundary condition $\frac{\partial \phi}{\partial x} = 0$ governs the potential at the inlet.

All walls are impenetrable, resulting in $\boldsymbol{F}_{+/-} \cdot \boldsymbol{n} = 0$ as well as $\boldsymbol{u} \cdot \boldsymbol{n} = 0$ in which $\boldsymbol{n}$ represents the surface normal vector of the respective wall—consequently, $\nabla c_{+/-} \cdot \boldsymbol{n} = \nabla \phi \cdot \boldsymbol{n} = \nabla p \cdot \boldsymbol{n} = 0$ applies.

Ideal CXMs are assumed with no anions being able to pass through the membrane, $F_{-,y} = 0$. Additionally, in line with previous research [38] we assume any convection of ions through the membranes, be it anions or cations, is negligible ($u_y = 0$).

The boundary conditions for both outlets are the same. In terms of the pressure, the Dirichlet condition $p = p_{\text{amb}} = 1 \times 10^5 \, \text{Pa}$ is prescribed. The outlet concentrations do not change, $\frac{\partial c_{+/-}}{\partial x} = 0$. Analogously to the inlet, the potential's gradient is zero in the x direction, $\frac{\partial \phi}{\partial x} = 0$.

B. Heterogeneous properties

We use a moderate nondimensionalized correlation length of $l = 0.1$ and employ a standard normal distribution for our autocorrelation function, leading to $\xi_0 = 1$ as our Gaussian autocorrelation factor. To improve numeric stability, a factor of 2/3 was multiplied to the random field z, narrowing the distribution. A total of six different random fields were generated, i.e., we pooled $\theta(\boldsymbol{k})$ from $\mathcal{U}(0, 2\pi)$ with six different random seeds. The distributions of the random fields are displayed in Fig. S1 of the Supplemental Material (SM) [59] alongside the resulting log-normal distributions (Fig. S2 and 2D spatial plots in Fig. S3).

Analogously to Mirzadeh *et al.* [43] we apply the exponential of the random field to our selected material properties. Instead of the hydrodynamic permeability, we chose the surface charge density, σ_{s}, as well as the porous area structure density, a_{p}; the base values of which are the constant factors in the paper of Schlumpberger *et al.* [38] and equate to γ_0 in Eq. (13). This is due to the fact that they represent fundamental variables in our model that propagate through our equations, affecting multiple other parameters such as k_{d} and k_{eo}. Our six random fields lead to a total of six runs per heterogeneous parameter we investigate. The heterogeneous structures for the porous structure area density and the surface charge density are displayed in Fig. 2.

C. Hierarchical media

Beyond the gradually changing materials of the previous section, we also analyze the effects of introducing hierarchical materials, similar to IERWs of previous experimental work [44–46]. We randomly generate areas, similar to particles, in the space between the CXMs with dimensions of 789 µm in the x direction and 506 µm in the y direction, which are allowed to overlap. Such
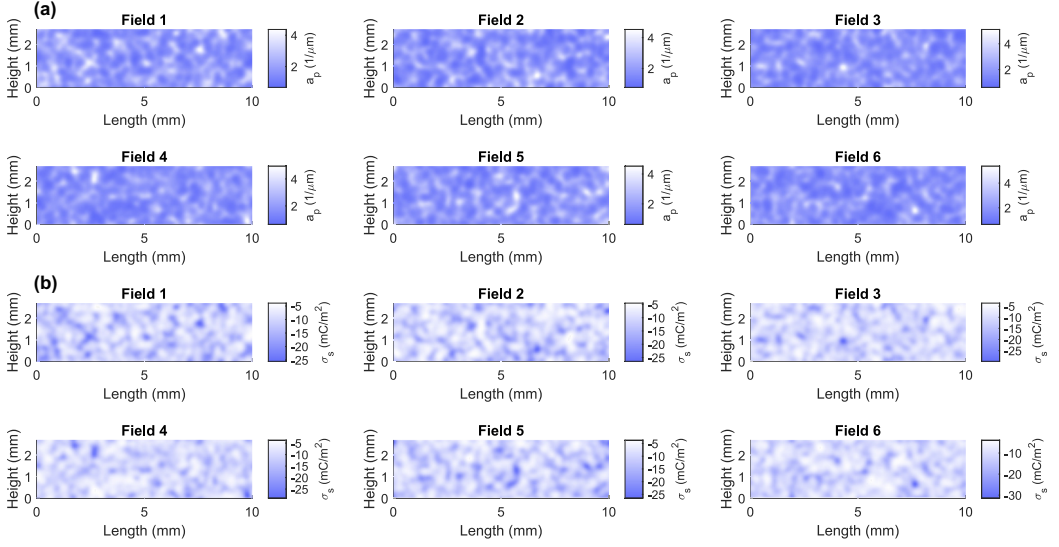
FIG. 2. Spatial distribution of (a) the heterogeneous porous structure area density a_p as well as (b) the surface charge density σ_s.

configurations could resemble particles bound by a binder, sintering of (bimodal) particles, or a sol-gel process of different types of particles.

For these new zones, the porosity is increased to 0.7 since IEX particles tend to possess higher void fractions [60]. Furthermore, a_p is increased by three factors of magnitude, signifying smaller pores. The diffusion coefficients are set to a tenth of their original value and we assume no electro-osmotic convection [39].

Outside of the particles' space, we retain the base case material properties to maintain a level of comparability with previous results but apply the heterogeneous fields to a_p.

D. Performance metrics

To understand the trade-offs in SED devices, we employ a set of metrics already applied in previous studies [38,39]. A specie's concentration in the diluate is calculated using the velocity-averaged values

$$c_{+/-,\text{diluate}} = \frac{\int_{S_{\text{diluate}}} c_{+/-} u_x \mathrm{d}S}{\int_{S_{\text{diluate}}} u_x \mathrm{d}S} \tag{18}$$

in which S is the surface to be integrated over.

Similarly, the degree of desalination is obtainable through

$$\chi = \frac{\int_{S_{\text{diluate}}} \sum c_i u_x \mathrm{d}S}{\int_{S_{\text{feed}}} \sum c_i u_x \mathrm{d}S}. \tag{19}$$

The energy consumption is quantified using

$$\varepsilon = \frac{IV + Q_{\text{feed}} \Delta p}{\omega Q_{\text{feed}}}. \tag{20}$$

It enables the comparison between different electrochemical methods, given the normalization by the diluate stream.

The pressure difference $\Delta p = \bar{p}_{\text{in}} - \bar{p}_{\text{out}}$ is approximated to be the delta between the average inlet's $\bar{p}_{\text{in}}$ and outlets' pressure $\bar{p}_{\text{out}}$. Using the mean values is a valid approximation as the pressure at the inlet or outlets should vary negligibly in the y direction for the present system and boundary conditions.

In Eq. (20), ω quantifies the water recovery, namely, the relation between the diluate stream and the feed stream,

$$\omega = \frac{Q_{\text{diluate}}}{Q_{\text{feed}}}, \tag{21}$$

with Q_{diluate} being the volumetric flow rate of the diluate stream,

$$Q_{\text{diluate}} = \int_{S_{\text{diluate}}} u_x \mathrm{d}S. \tag{22}$$

Besides the energy consumption, the current efficiency

$$\eta = \frac{z_+ e Q_{\text{diluate}}(c_{+,\text{feed}} - c_{+,\text{diluate}})}{nI} \tag{23}$$

is computed. In the context of this paper, the stack number n is always equal to 1. The conductance values are calculated from the slope of the current voltage curve at overlimiting conditions $\kappa = \frac{\Delta I}{\Delta V}$. The reported values are scaled by the theoretical surface conductance at zero flow for a homogeneous porous material with $\gamma_0(\boldsymbol{x}) = \epsilon_{\text{p},0} = 0.48$ [23,38,39]:

$$\tilde{\kappa} = \frac{\kappa}{\kappa_{\text{sc}}} = \kappa \frac{h_{\text{p}} H k T}{z_+ D_+ |\sigma| \epsilon_{\text{p}}^{1.5} W L e}. \tag{24}$$

The current I is calculated with

$$I = \int_{S_{\text{CXM}}} \sum z_i e F_{i,y}. \tag{25}$$

It can be nondimensionalized by $z_+ s_+ c_0 e Q_{\text{feed}}$ as done by Schlumpberger *et al.* [24]. Using the top or bottom membrane to evaluate the current leads to equivalent results in the herein investigated system.

When comparing solutions of nonbinary electrolytes, it is important to identify the selectivity that we define for a species i and j as

$$S = \frac{\frac{c_i}{c_{i,0}}}{\frac{c_j}{c_{j,0}}} \tag{26}$$

in which c_0 signifies the concentration at the inlet [27,44].

IV. RESULTS AND DISCUSSION

A. Base case: No heterogeneity

To provide a baseline and capture the effects of the new inlet and outlet geometry, we simulate the results of the system for a homogeneous base case, i.e., no heterogeneous parameters and all properties according to Schlumpberger *et al.* [38]. Table II includes select performance metrics such as the energy consumption, water recovery, current efficiency, and pressure drop at varying ion removal fractions. These provide a framework for comparing trade-offs in subsequent cases when, e.g., materials possess heterogeneous properties. In addition, Fig. S4 visualizes the respective cation concentration, potential, as well as pressure fields.

The results mimic those reported by preceding research [38,39], including a substantial increase in energy consumption taking place from 80% to 99% ion removal. With an expanding depletion

TABLE II. Performance metrics for the homogeneous base case. The energy consumption ε, water recovery ω, current efficiency η, and pressure drop Δp across the device for 80%, 90%, as well as 99% ion removal are recorded.

Metric	Ion removal		
	80%	90%	99%
Energy consumption (kJ L^{-1})	2.30	3.85	9.97
Water recovery (%)	52.02	54.32	66.20
Current efficiency (%)	54.81	53.77	49.41
Pressure drop (kPa)	23.40	23.30	22.68

zone, the influence of the EOF increases due to the developing potential gradient [40], causing the flow to arch down near the outlet and the depletion zone to decrease as $x \rightarrow L$ [39].

Analogously to counter-rotating vortices that establish themselves in an individual pore or channel [33], an opposing pressure-driven flow (PDF) balancing the EOF will form near an ion-selective interface on a macroscopic level. As described by Tian *et al.* [39], this disrupts the uniformity of the velocity field, forming circulatory flow patterns—up to vortices—which drive an increased amount of fluid through the outlet but concurrently transport brine downwards. Hence, the depletion zone does not increase monotonically, causing higher concentrations in the outlet and necessitating more energy be invested for higher ion removal. At the same time, the water recovery exceeds the value of 50% for uniform flow, with the side effect of lowering the pressure drop Δp.

The pressure drop also influences the energy consumption [see Eq. (20)]; yet, its contribution ($< 1\%$) is negligible compared to the electrical power. Therefore, the overall energy consumption is not reduced. Tian *et al.* [39] have previously reported a vortex near the inlet. We do not observe such a second pattern, likely due to the differences in geometry. Additionally, the explicit modeling of the electrolyte channels and membranes around the SED cell as done by Tian *et al.* [39] could have an influence. An increase in pressure near the inlet is, nevertheless, noticeable, especially for 99% ion removal.

The conductance of $\tilde{\kappa} = 1.10$ is slightly higher than the theoretical OLC value, which scales with the surface charge density [23,36], but less than experimentally measured. A differentiator could be that we do not include hydronium transport in our model [39]. In terms of current efficiency, the results are in the previous experimental and modeling range [24,39]. Overall, our new geometry does not change the underlying trends of previous studies.

B. Heterogeneous material properties

Following the base case, we turn our attention to the effects of heterogeneous material properties. The six random field distributions are applied to the porous structure area density a_p and the surface charge density σ_s as displayed in Fig. 2.

1. SED performance for a heterogeneous porous structure area density

As an example, Fig. 3 displays the dimensionless cation concentration, pressure, and potential alongside the streamlines and normalized fluxes for run 6 (i.e., applying the log-normal distribution of field 6 to a_p). As can be seen, the effects of introducing heterogeneity are very distinct.

The depletion zone possesses an uneven border, visible in the concentration and potential field. Alizadeh *et al.* [40] have previously reported this for their results when analyzing random networks of distinct pores. That being said, the general structure of the depletion zone is preserved as it expands. The spike, distinguishable for the cation concentration as well as the potential between $x = 7$ and 8 mm, for example, remains present from 80% to 99% ion removal. This speaks for some stability even with a seemingly chaotic flow.
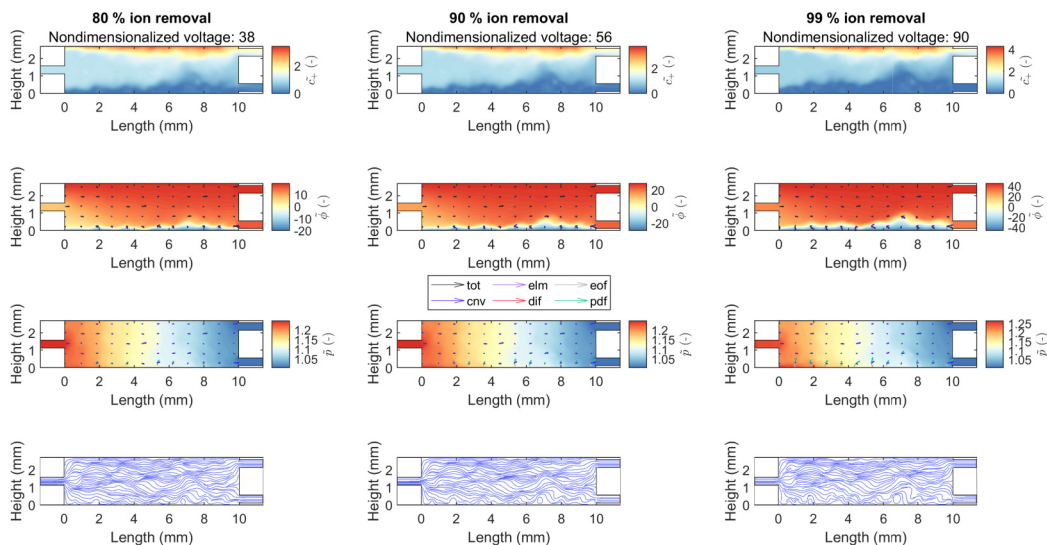
FIG. 3. Dimensionless cation concentration, pressure, potential, and streamlines at varying ion removal fractions for the heterogeneous porous structure of run 6. The total (tot), convective (cnv), diffusive (dif), and electromigrative (elm) fluxes are included with the potential. Along with the pressure, the electro-osmotic flow (eof) and the pressure-driven flow (pdf) contributions to the convective flux are shown. All fluxes are in relation to the cations and normalized by their concentration.

Looking at the streamlines it becomes evident that the depletion zone mimics the underlying flow in the system. Multiple vortices form at the cation exchange membrane (the ion-selective interface). These drive brine down or push the depleted electrolyte up, causing the jagged shape.

As the depletion zone expands, the extent and number of vortices increases, which can also be seen in video 7 of the SM. Once again this is attributable to the growing relative influence of the EOF as the potential gradient increases, as will be elaborated later on.

To better illustrate and explain the effects of $a_p \neq$ const, Fig. 4 provides the performance metrics for the six random distributions in comparison to the base case for 80%, 90%, and 99% ion removal. As the required applied voltage increases, differences in the metrics are exacerbated. Since the most substantial variability appears to exist between run 2 and run 4, we present the cation concentration and fluxes as well as the porous structure area density and streamlines for them in Fig. 4.

Consistently, the homogeneous base case demonstrates the highest water recovery (yield) as well as current efficiency irrespective of the ion removal fraction, i.e., applied voltage. In contrast to the homogeneous base case, more chaotic flows develop near the outlet. Fully formed vortices along the length of the SED cell also drive fluid upwards. Depending on the eddies' positions, the results of the PDF cannot be counteracted by the strong EOF near the outlet, as demonstrated by the streamlines of run 2. The vortex immediately before the bottom outlet transports fluid up and past the exit. In run 4, on the other hand, the chaotic flow that forms leads to a flow field in which electrolyte is diverted towards the outlet, similar to the homogeneous base case. In sum, though, the high number of eddies leads to overall lower yields.

The water recovery also influences the current efficiency via the bottom outlet's flow rate Q_{diluate}. Since $\eta \sim \frac{Q_{\text{diluate}} \Delta c}{I}$, higher water recoveries promote improved efficiencies as long as the currents are in a similar range at equal depletion. Since at 99% ion removal the current for run 2 becomes very high, the efficiency drops below the result for run 4, in spite of the relatively substantial water recovery. Nonetheless, the overall low efficiencies are largely a result of higher currents, resulting
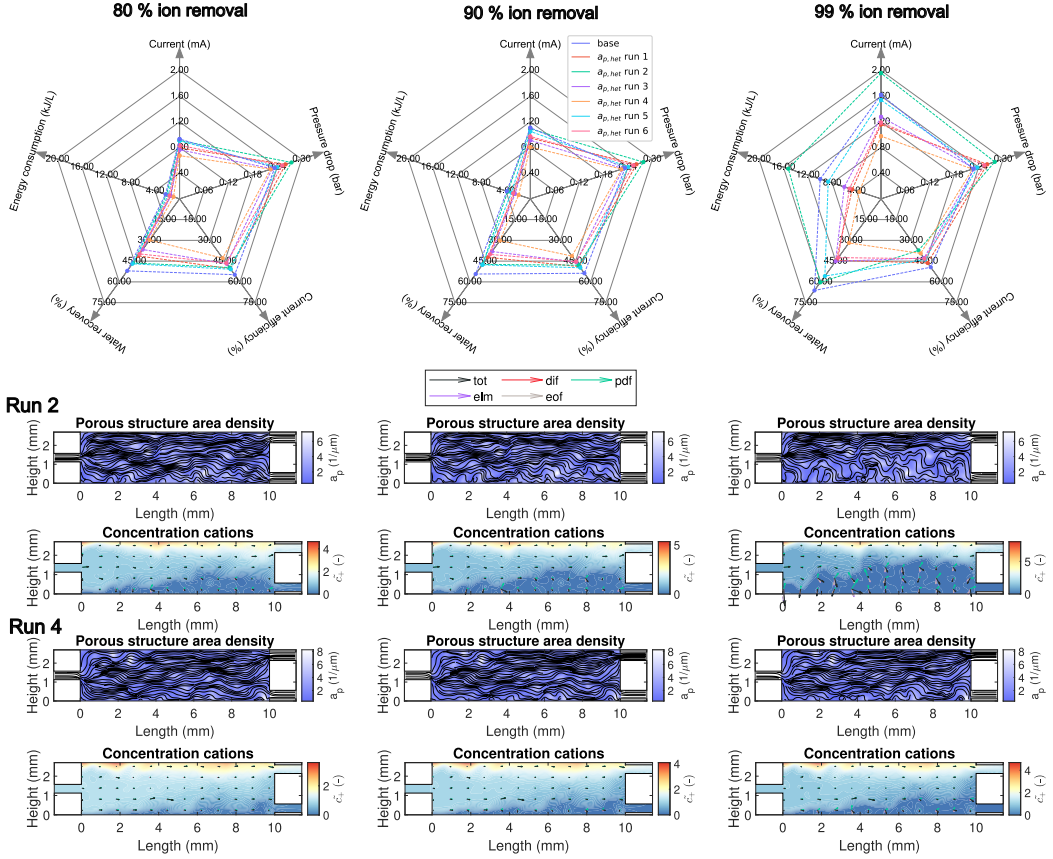
FIG. 4. Results and performance metrics for a heterogeneous porous structure area density a_p at varying ion removal fractions. The current, pressure drop across the SED cell, current efficiency, water recovery, and energy consumption are displayed for the six runs with varying a_p distributions in comparison to the homogeneous base case at 80%, 90%, and 99% removal of ions. Simultaneously, the relation between the streamlines and a_p for runs 2 and 4 are captured, alongside the dimensionless cation concentration $\tilde{c}_+$ profile and fluxes scaled by the cation concentration.

from mixing of brine and diluate through the vortices, which increase the OLC but not the ion removal (see Fig. S5).

As expected, the formation of vortices leads to higher Δp across the SED cell. The pressure difference contributes minimally to the overall energy consumption, but if instead a stack of SED cells were to be employed, the pressure drop would become relevant. In general, the energy consumption and currents are lower than for the homogeneous base case, with the exception of run 2 at 99% ion removal. Comparing Fig. S4 and Fig. 4 this is also evident by the lower dimensionless voltages for run 6 to achieve equivalent ion removal [see Eq. (20)]. Nevertheless, the inherent trade-off between water recovery and energy consumption appears to persist [24]—an important economic consideration for future implementations. Run 2 also demonstrates that with certain heterogeneous media in the SED cell, it is possible to perform poorer both in terms of water recovery and energy consumption. Accordingly, it is important to understand the influences of the porous structure in more detail.

2. Effects of a heterogeneous porous structure area density on flow

Described by Deng *et al.* [23]—then further elaborated and demonstrated in the work of Alizadeh *et al.* [40] and Mirzadeh *et al.* [43]—heterogeneities in the porous structure lead to vortex formation through the interaction of opposing EOF and PDF. In contrast to effects in homogeneous materials, flow patterns stretch beyond an individual pore and are dependent on the depletion zone, in addition to the extent of the heterogeneities, i.e., the correlation length. Differences in hydrodynamic permeability due to varying pore sizes, lead to vortices where EOF follows the path of high, and the opposing PDF the path of low hydrodynamic resistance [23,40,43]. As we can see, such phenomena can become the determining mechanism for electrokinetic transport.

Since $a_p \sim 1/h_p$, the flow will be directed due to EOF towards the bottom membrane in regions of high a_p and where a_p is low, diverted from the bottom membrane, as the PDF follows the path of highest permeability—illustrated by the fluxes and streamlines in relation to the porous structure area density for run 2 and run 4.

Accordingly, differences in a_p explain the reduced energy consumption and water recovery of run 4. As previously mentioned, the root cause for the low metrics is the vortex that forms immediately before the diluate exit. Near the outlet, a region of rather high a_p is present, similar in size to the exit's dimensions, surrounded by a connected region of low a_p that ends above the outlet. The consequence is a vortex shortly before the exit, where in the regions of low a_p PDF pushes water past it. The EOF drives very depleted electrolytes through the outlet but cannot counteract the general trend of the PDF resulting in a diminished water recovery. In run 2, on the other hand, higher values for a_p near the exit are located further away from the bottom membrane, possess substantially lower values, and are more diffuse. The resulting two vortical flow patterns transport the nondepleted fluid down and through the outlet, which can be seen in video 3 of the SM in the height-averaged concentration profile. Therefore, higher voltages need to be applied, simultaneously causing the eddies in the SED cell to expand with the overall depletion zone and leading to a very chaotic flow. Considering the length-averaged concentration profiles of video 3, a strong resemblance to mixing layers of electro-osmotic instabilities (EOIs) can be discerned, further hindering depletion [61].

The differences in flow patterns are also reflected in the dimensionless conductance. Run 2 possesses a value of 1.37, while run 4 has a value of 1.09. The eddies formed by run 2 transport more ions towards the bottom membrane, therefore, increasing the overlimiting current. Since the depletion zone for run 4 is enhanced, an almost equivalent conductance to the homogeneous base case is recorded.

Given the high dependence of the metrics on the flow, the effects of a varying volumetric surface charge density $\rho_s \sim 1/h_p$ [see Eq. (9)] appear negligible. An important factor to consider, however, appears to be the heterogeneity of the outlet region and its impact. Qualitative analyses, as done in the previous paragraphs, should be replaced in the future by quantitative computations based on the underlying a_p distribution, so that precise predictions leading to design decisions are possible.

3. SED performance for a heterogeneous surface charge density

Besides heterogeneity in the geometry of the porous media utilized in SED or other electrokinetic applications, the surface charge density σ_s can vary, e.g., due to the distribution of surface functional groups.

Figure 5 provides an overview of the performance metrics, when applying the six random fields to the surface charge density, alongside more detailed results of runs 1 and 3.

Overall, the variance between runs is much lower than for the heterogeneous porous structure area density cases. Up until 99% ion removal, the $\sigma_{s,het}$ metrics are almost equivalent, with the most substantial changes recorded for the energy consumption and water recovery. Both the pressure drop and current efficiency do not deviate much from the values of the homogeneous base case. Considering Eq. (20), it is understandable that the trends in the current itself are reflected to a large degree in the energy consumption.
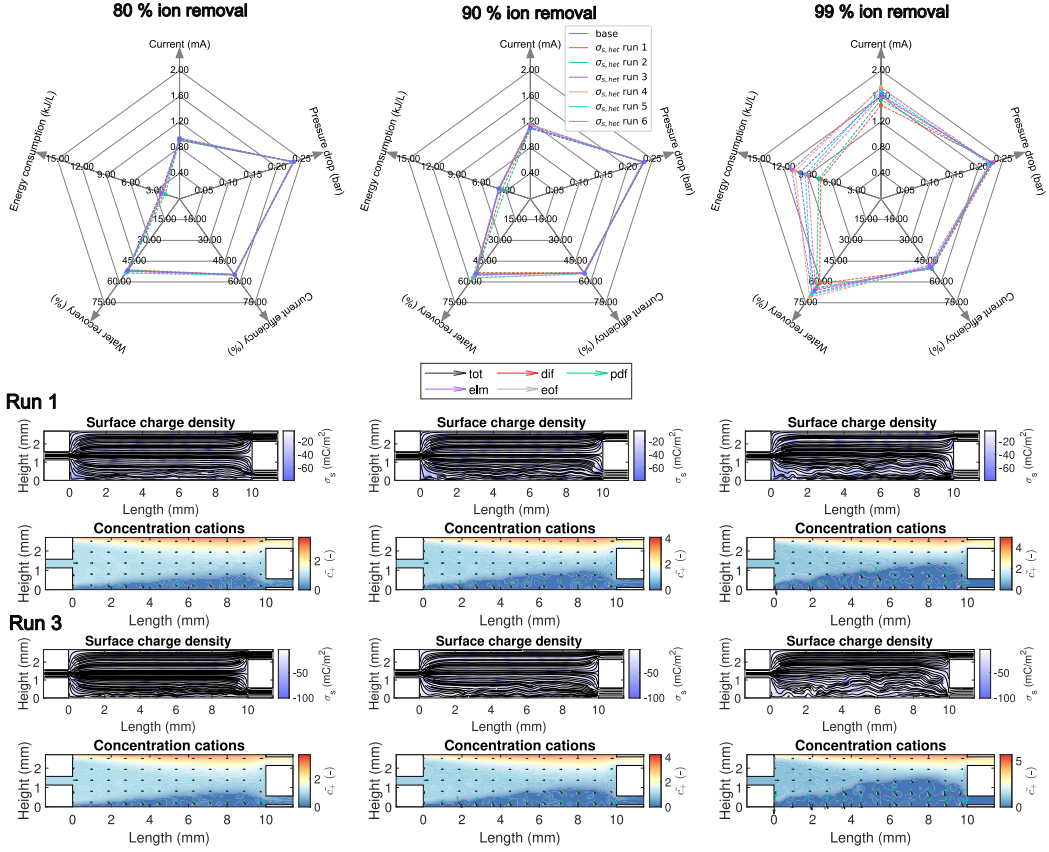
FIG. 5. Results and performance metrics for a heterogeneous surface charge density σ_s at varying ion removal fractions. The current, pressure drop across the SED cell, current efficiency, water recovery, and energy consumption are displayed for the six runs with varying σ_s distributions in comparison to the homogeneous base case at 80%, 90%, and 99% removal of ions. Simultaneously, the relation between the streamlines and σ_s for runs 1 and 3 are captured, alongside the dimensionless cation concentration $\tilde{c}_+$ profile and fluxes scaled by the cation concentration.

Visible from the streamlines of both runs, the similarity to the homogeneous base case largely stems from the comparatively small perturbation of the flow field. Primarily at 99% ion removal, vortexlike structures become prevalent, thereby, causing larger differences in the metrics. The less chaotic flow leads to generally lower conductance values than for $a_{p,het}$, recorded in Table III. The largest conductance originates in run 5 for which video 12 of the SM reveals a flow field with electrolytes of higher concentration transported to the bottom membrane.

Contrary to the heterogeneous porous structure area density results, the clear trade-off between energy consumption and water recovery does not emerge for the heterogeneous surface charge density. Instead, as run 5, for example, demonstrates, a lower energy consumption at higher water recovery is obtainable. Since the flow is less chaotic, the depletion zone forms more monotonically, thereby increasing the conductance slightly without causing adverse mixing or outlet vortex effects.

Importantly, as displayed in Fig. 6, even for the cases in which the water recovery is lower than the homogeneous base case, higher currents or voltages can be applied after 99% ion removal to reach equivalent yields while using less energy. Therefore, the water recovery can still be increased while maintaining a lower energy input.

TABLE III. Dimensionless conductance values for the heterogeneous surface charge density $\sigma_{s,het}$ and porous structure area density $a_{p,het}$ runs. The conductance was obtained from the slope of the current-voltage curve at overlimiting current and then scaled by the idealized value [Eq. (24)]. The dimensionless conductance for the homogeneous base case is 1.11.

Run no.	Dimensionless conductance ($\sigma_{s,het}$)	Dimensionless conductance ($a_{p,het}$)
1	1.15	1.56
2	1.26	1.37
3	1.08	1.40
4	1.24	1.09
5	1.37	1.42
6	1.16	1.40

This is not possible for the heterogeneous porous structure area density as displayed in Fig. S5 of the SM. The chaotic flow, while reducing the energy consumption substantially in certain configurations, diminishes the water recovery too significantly to reach the homogeneous base water recovery values at comparable energy input.

4. Effects of a heterogeneous surface charge density on flow

Mirzadeh *et al.* [43] pointed out that next to the heterogeneity they introduced in the permeability tensor for the hydrodynamic resistance, the electro-osmotic permeability could also lead to similar vortical flow patterns if irregularly distributed in the porous media. As evident from Eq. (4), varying the surface charge density affects k_{eo}. However, the electro-osmotic permeability for our chosen material properties is generally lower than k_d, in addition to σ_s and k_{eo} not exhibiting the quadratic relationship of a_p and k_d. As a consequence, the flow is less perturbed, which leads to fewer vortices and smoother depletion zone borders. The relationship between σ_s and k_{eo} is displayed in Fig. S6 in the SM.

Comparing runs 1 and 3, the effects of varying the surface charge density, and thereby the electro-osmotic permeability, become evident. Since higher absolute values of the surface charge density lead to lower values for the electro-osmotic permeability, the streamlines arch down towards the membrane in sections of lower $|\sigma_s|$. Those regions exhibit a reduced electro-osmotic resistance and
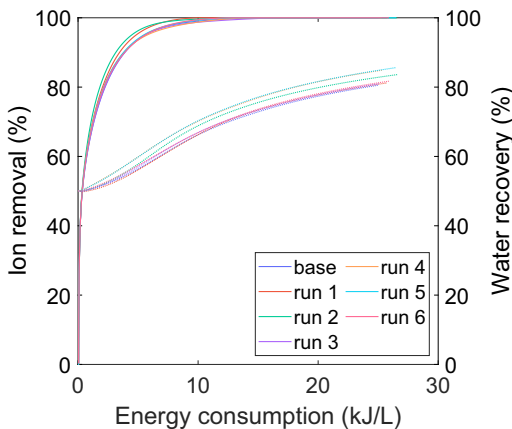

FIG. 6. Ion removal and water recovery with increasing energy consumption for SED cells with a heterogeneous surface charge density, σ_s.

are, therefore, preferred by the EOF. The PDF for $k_d = \text{const}$ has no favored pathways of high permeability. Consequently, the opposing PDF follows regions of high $|\sigma_s|$.

Between runs, the velocity fields are aligned more closely than for the heterogeneous a_p simulations, and substantial changes appear at high ion removal fractions. With the effects of the absolute value of the surface charge density $|\sigma_s|$ in mind, a qualitative discussion is possible. For run 1, a region of high $|\sigma_s|$ exists near the outlet and located slightly above the bottom membrane. Analogously to run 4 of the heterogeneous porous structure area density, the typical flow that arches down towards the outlet is hindered by an opposing PDF, reducing the water recovery as well as preventing substantial amounts of higher concentrated electrolyte to be dragged down into the depletion zone. In video 8 of the SM, it is discernible that at potentials past the point of 99% ion removal, an almost horizontal barrier of depleted electrolyte forms just above the exit.

In run 3, on the other hand, a low $|\sigma_s|$ region is present close to the outlet. Consequently, EOF will transport brine down and through the exit, reducing the depletion and increasing the water recovery. At $x \approx 9$ mm a region of higher $|\sigma_s|$ exists that counteracts some of the downward flow, which could explain why the water recovery in comparison to runs 4 and 5 is lower. Additionally, run 3 exhibits the least conductance, which is likely another contributing factor to the higher energy consumption.

Even though the flow for a heterogeneous σ_s does not display the same extent of chaotic patterns as observed for variance in a_p, videos 8–13 of the SM hint at the formation of mixing layers for high applied potentials based on the height-averaged concentration profiles [61].

Nevertheless, in many instances the introduction of heterogeneity in the surface charge density can be beneficial or be used to drive the system to favor one metric over another—without altering the SED cell's geometry. Consequently, choosing the proper material functionalization might lead to better performing SED or similar electrokinetic devices in the future.

C. Hierarchical media

Building upon the previous sections, we introduce geometrical hierarchy into the porous material. Alizadeh *et al.* [40] modeled networks of pores of different diameters explicitly. Here we present a macroscopic approach in which we introduce regions of high homogeneous porous structure area density, i.e., particles with small pores but high porosity, into the previous heterogeneous a_p fields (akin to a charged, porous, heterogeneous binder circumferencing the particles). This is in loose analogy to the IERWs employed in experiments by Alkhadra *et al.* [44] for shock ion extraction.

From Fig. 7(a) it becomes apparent that the current-voltage relationship differs substantially from the homogeneous base case and is heavily dependent on the hierarchical structure, stemming both from the heterogeneity in the binder a_p as well as the presence of the particles. Due to numerical difficulties at high desalination, not every run could be modeled to the maximum applied voltage of the base case, but all runs achieved 99% ion removal.

Throughout the examples, higher currents than for the homogeneous base case as well as the heterogeneous materials of the previous sections are recorded. Given the streamlines of Fig. 7(d), the chaotic, vortical flow, along with the increased volumetric surface charge density ρ_s of the particles [36], lead to the altered IV curve. Furthermore, there exist higher degrees of deviation from linearity in the IV curve at OLC compared to the prior cases (see Fig. 6 and Fig. S5). Seemingly tied to this, is a less distinct transition to an OLC regime that takes place at higher voltages. Deng *et al.* [23] had observed a more gradual transition when positioning the frit in a way that natural convection was mitigated and instead diffusive effects became more prevalent. Considering the large concentration differences and fluxes of Fig. 7(d), diffusion at the interface to the particles increases in relative importance and could contribute to a less distinct transition to OLC. The change in curvature around 4 V for run 1 and slightly noticeable with run 6 as well could indicate that.

Evident from Figs. 7(b) and 7(c), the latter of which shows the metrics for 99% ion removal, we cannot record better performance through the introduction of hierarchical structures, contrary to Alkhadra *et al.* [44]. With the exception of run 3, the energy consumption to achieve a comparable depletion is higher than for the homogeneous base case. Even for run 3 this is not the case prior
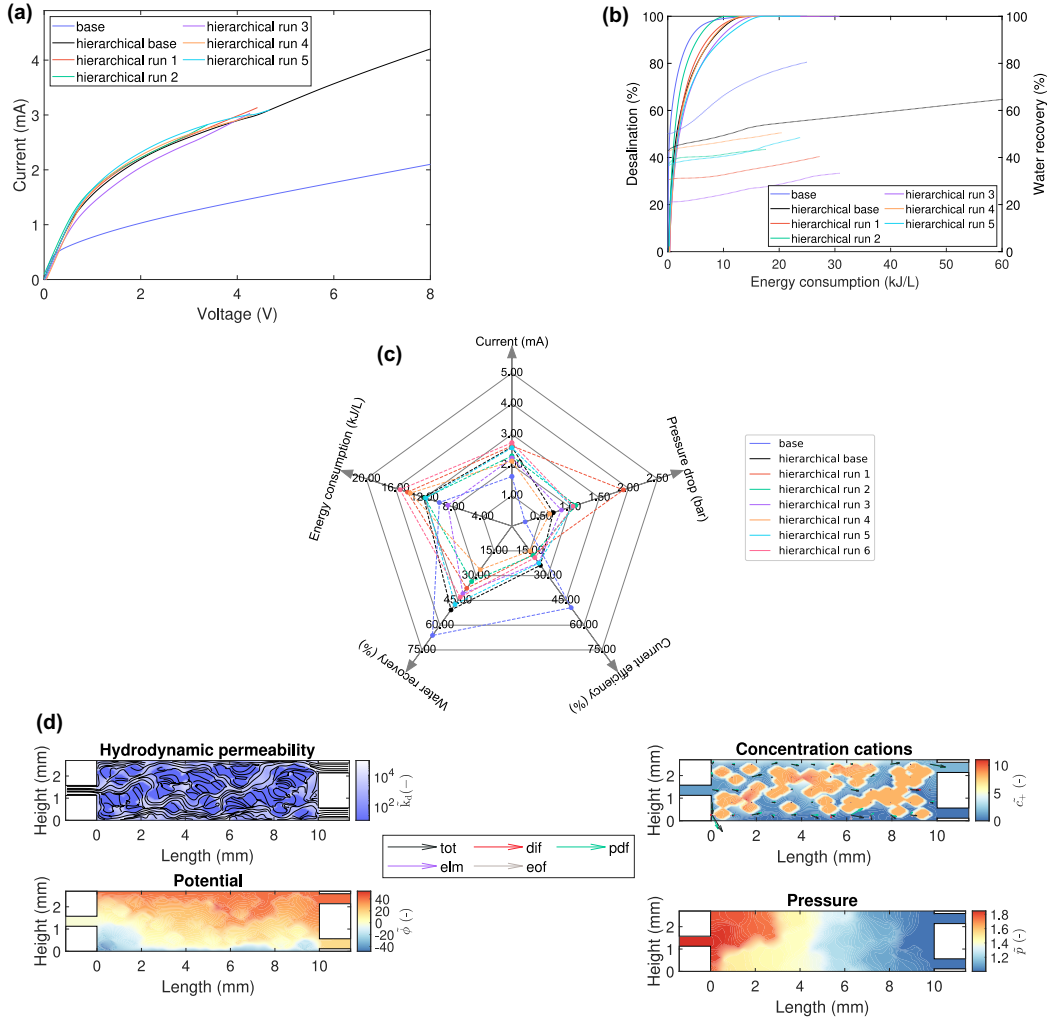
FIG. 7. Effects of hierarchical geometric structures in porous materials for SED. The homogeneous base case, the case with particles but no heterogeneity in the surrounding material (binder), as well the six runs using the previous heterogeneous porous structure area density distributions for the nonparticle regions are compared: (a) the current-voltage relationship, (b) the ion removal and water recovery in dependence of the energy consumption, (c) the performance metrics for 99% ion removal, and (d) the streamlines in relation to the dimensionless hydrodynamic permeability, as well as the dimensionless cation concentration, potential, and pressure for run 3 at 99% ion removal.

to approximately 98% ion removal as demonstrated by Fig. 7(b). Moreover, for all cases the water recovery is substantially lower as the particles, especially near the bottom outlet, divert the flow. The water recovery also exhibits substantially less variability in dependence of the energy input than in prior cases. This also holds true for the alternate particle distribution of Fig. S7 of the SM, in which a different chaotic flow hinders low energy consumption at high water recoveries. Lower water recoveries than with nonhierarchical media had also been observed by Alkhadra *et al.* [44], though we do not see it decrease with current.

As can be expected, the pressure drop increases substantially given the now higher hydrodynamic resistance, which can be seen in the pressure field of Fig. 7(d). The effect on the energy consumption is still low but should be considered in a scaled-up stack configuration.

Interestingly, many of the runs perform better than the case for which no heterogeneity is present in the binder regions. The altered flow patterns are beneficial in removing a high degree of ions at low energy consumption without sacrificing yield. This is different from the results of the previous sections surrounding the effects of varying a_p. However, in the case of the particles, even the homogeneous binder property results already experience vortical flow due to the particles.

Even though our model is highly idealized and will need to be refined in future work to capture the full effects of IERWs, especially concerning the electrostatic interactions, we can see that the underlying structure of the porous material appears to exert a strong influence. The same particle configuration, but varying heterogeneity of a_p in the binder, results in substantial differences in performance. Consequently, the syntheses of materials such as IERWs should strongly consider the effects particle positioning and binder porosity have. Furthermore, it seems vital to include the surface charge—possibly also exchange kinetics—to provide simulations with results close to experimental data.

D. Selectivity in heterogeneous media

Returning to heterogeneity in a_p as well as σ_s, we aim to understand whether this may affect selectivity. Separation of charged compounds could be a primary application for utilizing depletion shocks, which requires the selective isolation of species. Alkhadra *et al.* [25], Conforti and Bazant [27] and Tian *et al.* [26] have demonstrated the selectivity for different cations in SED—both experimentally and through simulations—based on the variation in interactions of mono- vs multivalent cations with the negatively charged pores and the CXM. Here, we analyze the selectivity towards anions for simplicity.

Since we are using a homogeneous model, are not modeling the membranes themselves, and highly simplifying any interactions surrounding the electrical double layer (EDL), analyzing anions should not come at a significant loss of information in comparison to cations. At the same time this enables the continued use of our modeling framework, including boundary conditions, defined in Sec. III. A drawback of this approach is the negligence of selectivity through the membrane, which may be covered in future models [39].

We analyze the selectivity for a monovalent (Cl^-) and a divalent (SO_4^{2-}) anion in a model electrolyte of magnesium, chloride, and sulfate. Figure 8 shows the selectivity [see Eq. (26)] of the diluate outlet stream with increasing applied voltage in comparison to the water recovery. For the heterogeneous materials the same configurations as in the previous sections are employed (see Fig. 2).

The results of Tian *et al.* [26] have shown that in a homogenized model, such as ours, differences in selectivity arise especially for lower concentrations, i.e., at higher applied voltages and depletion of the electrolyte. Our simulation results follow the same trend but our selectivity values are likely too high as a result of the aforementioned simplifications.

Nonetheless, for the challenging problem of isolating dilute species, changes in selectivity heavily depend on the underlying heterogeneity as evident in the various runs. Moreover, the heterogeneous porous structure area density causes larger deviations from the trends of the homogeneous base case than a varying surface charge density. This is explicable given the previous sections' results. With our model setup, selectivity arises through differences in mobility, resulting from variations in diffusivity and valence, of which the effects will be stronger for a more vortex dominated flow [27]. Furthermore, in many of the previous cases, a higher desalination at lower applied voltages was achieved. Given that selectivity increases for lower concentrations this, too, contributes to the differences.

Generally, the runs for which the flow was previously more chaotic, such as run 2 or run 5, demonstrate lower selectivity at comparable voltages than, e.g., run 4. As the flow becomes more chaotic, mixing effects will increase [40], which reduces depletion as well as selectivity.

Contrary to the previous results, there exists less of a trade-off with respect to the water recovery, especially at higher applied voltages, possibly due to the lower inlet concentration and resulting
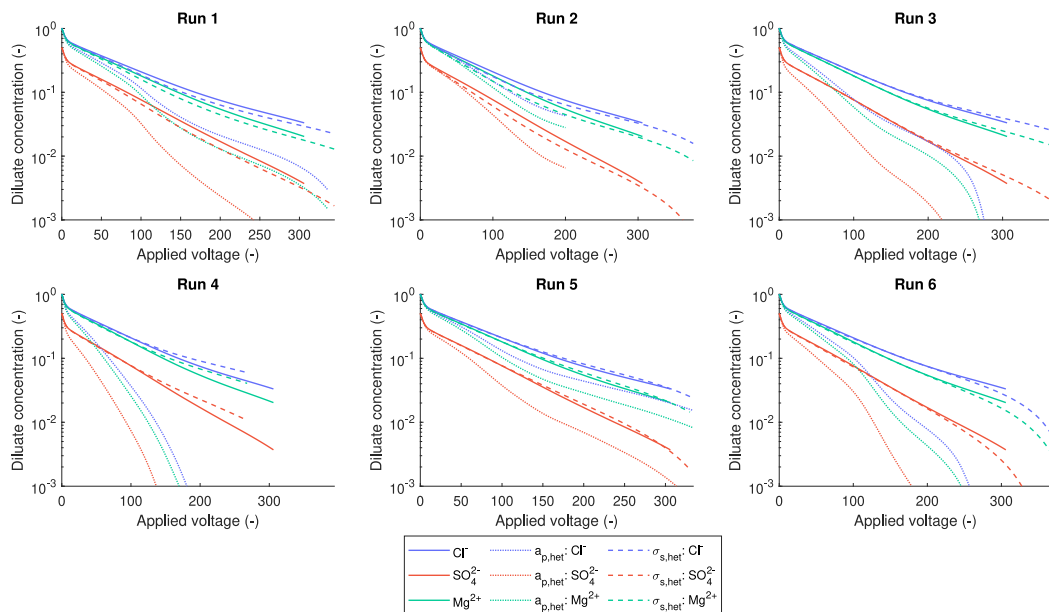
FIG. 8. Effects of heterogeneity in the porous structure area density a_p or surface charge density σ_s for the selectivity of chloride, Cl^-, and sulfate, SO_4^{2-}, ions in SED. Displayed is the fresh outlet's concentration of the individual species with increasing applied potential. The positive counterion is magnesium, Mg^{2+}.

absolute surface charge density [39]. Even though the water recovery might be slightly lower for heterogeneous materials, in applications of SED, the gains in selectivity would likely be more important.

Irrespective of these results, it should be mentioned that Alkhadra *et al.* [44] and Tian *et al.* [26] have demonstrated the important role the EDL plays with respect to selectivity. More advanced models for charge regulation and interactions should be considered, particularly for bi- or multimodal surface charge density distributions as they are present in IERWs, which exhibit high selectivity [44]. Heterogeneity in the charge and structure of the porous media may both contribute to an increased selectivity.

V. CONCLUSION AND OUTLOOK

We have introduced heterogeneous material properties in a crossflow SED simulation, observing varying degrees of vortex formation with broad effects on performance and selectivity. The size of the eddies is, hereby, heavily dependent not only on the underlying material properties that influence the permeability but also on the extent of the depletion zone. Especially variations near the outlet have a profound impact.

Geometric heterogeneity, including hierarchical structures, frequently leads to very chaotic, vortical flow which often reduces the overall performance. A nonhomogeneous surface charge density, on the other hand, can reduce in many instances the energy consumption while still retaining yields. Accordingly, future concentration shock simulation studies should employ adapted models that incorporate greater detail with respect to the EDL interactions. New simulations may then also describe the results of shock ion extraction, which our current implementation does not fully capture. Adjustments surrounding charge regulation and ion exchange kinetics of the resin beads might be necessary. A more detailed molecular interaction analysis would provide more insight into the governing principles at the interface.

We have, nevertheless, demonstrated the strong influence heterogeneity in the binder between ion exchange particles can have. Additionally, we have shown that heterogeneous geometrical structures may benefit selectivity, especially for dilute solutions.

Alongside experimental work and simulations, future studies should follow the tradition of SED research and work towards analytical expressions as well as new scaling relations for heterogeneous materials, so that fast design decisions may be made. Herein, techniques from turbulence modeling could be of value when characterizing the effects of vortices.

Overall, this study has shown the complexity and opportunities that exist for conceptualizing porous materials utilized in electrochemical methods. Even with simplified assumptions, complex behavior is observed that can be exploited in the next generation of materials. With a controlled synthesis, our results point towards an opportunity of effectively mitigating the trade-off between energy consumption and yield through heterogeneous porous structures, while possibly increasing selectivity.

[1] Transforming our world: the 2030 agenda for sustainable development, A/res/70/1, 2015.

[2] N. P. Hankins and R. Singh, *Emerging Membrane Technology for Sustainable Water Treatment* (Elsevier, Amsterdam, 2016).

[3] L. Bazinet and T. R. Geoffroy, Electrodialytic processes: Market overview, membrane phenomena, recent developments and sustainable strategies, Membranes **10**, 221 (2020).

[4] M. A. Abdelkareem, M. El Haj Assad, E. T. Sayed, and B. Soudan, Recent progress in the use of renewable energy sources to power water desalination plants, Desalination **435**, 97 (2018).

[5] F. Esmaeilion, Hybrid renewable energy systems for desalination, Appl. Water Sci. **10**, 84 (2020).

[6] A. Kasaeian, F. Rajaee, and W.-M. Yan, Osmotic desalination by solar energy: A critical review, Renewable Energy **134**, 1473 (2019).

[7] D. Curto, V. Franzitta, and A. Guercio, A review of the water desalination technologies, Appl. Sci. **11**, 670 (2021).

[8] M. A. Alkhadra, X. Su, M. E. Suss, H. Tian, E. N. Guyes, A. N. Shocron, K. M. Conforti, J. P. de Souza, N. Kim, M. Tedesco, K. Khoiruddin, I. G. Wenten, J. G. Santiago, T. A. Hatton, and M. Z. Bazant, Electrochemical methods for water purification, ion separations, and energy conversion, Chem. Rev. **122**, 13547 (2022).

[9] S. Bolisetty, M. Peydayesh, and R. Mezzenga, Sustainable technologies for water purification from heavy metals: Review and analysis, Chem. Soc. Rev. **48**, 463 (2019).

[10] M. E. Suss and V. Presser, Water desalination with energy storage electrode materials, Joule **2**, 10 (2018).

[11] N. Mir and Y. Bicer, Integration of electrodialysis with renewable energy sources for sustainable freshwater production: A review, J. Environ. Manage. **289**, 112496 (2021).

[12] A. Al-Karaghouli and L. L. Kazmerski, Energy consumption and water production cost of conventional and renewable-energy-powered desalination processes, Renewable Sustainable Energy Rev. **24**, 343 (2013).

[13] L. Gurreri, A. Tamburini, A. Cipollina, and G. Micale, Electrodialysis applications in wastewater treatment for environmental protection and resources recovery: A systematic review on progress and perspectives, Membranes **10**, 146 (2020).

[14] V. Silva, E. Poiesz, and P. van der Heijden, Industrial wastewater desalination using electrodialysis: Evaluation and plant design, J. Appl. Electrochem. **43**, 1057 (2013).

[15] H. Strathmann, Electrodialysis, a mature technology with a multitude of new applications, Desalination **264**, 268 (2010).

[16] E. Güler, W. van Baak, M. Saakes, and K. Nijmeijer, Monovalent-ion-selective membranes for reverse electrodialysis, J. Membr. Sci. **455**, 254 (2014).

[17] M. Irfan, L. Ge, Y. Wang, Z. Yang, and T. Xu, Hydrophobic side chains impart anion exchange membranes with high monovalent–divalent anion selectivity in electrodialysis, ACS Sustainable Chem. Eng. **7**, 4429 (2019).

[18] S. Kadel, G. Pellerin, J. Thibodeau, V. Perreault, C. Lainé, and L. Bazinet, How molecular weight cut-offs and physicochemical properties of polyether sulfone membranes affect peptide migration and selectivity during electrodialysis with filtration membranes, Membranes **9**, 153 (2019).

[19] L. Bazinet and M. Araya-Farias, Effect of calcium and carbonate concentrations on cationic membrane fouling during electrodialysis, J. Colloid Interface Sci. **281**, 188 (2005).

[20] L. J. Banasiak and A. I. Schäfer, Removal of inorganic trace contaminants by electrodialysis in a remote Australian community, Desalination **248**, 48 (2009).

[21] M. Z. Bazant, E. V. Dydek, D. S. Deng, and A. Mani, Desalination and purification system (U.S. Patent No. 8,999,132), U.S. Patent and Trademark Office (2015).

[22] A. Mani and M. Z. Bazant, Deionization shocks in microstructures, Phys. Rev. E **84**, 061504 (2011).

[23] D. Deng, E. V. Dydek, J.-H. Han, S. Schlumpberger, A. Mani, B. Zaltzman, and M. Z. Bazant, Overlimiting current and shock electrodialysis in porous media, Langmuir **29**, 16167 (2013).

[24] S. Schlumpberger, N. B. Lu, M. E. Suss, and M. Z. Bazant, Scalable and continuous water deionization by shock electrodialysis, Environ. Sci. Technol. Lett. **2**, 367 (2015).

[25] M. A. Alkhadra, K. M. Conforti, T. Gao, H. Tian, and M. Z. Bazant, Continuous separation of radionuclides from contaminated water by shock electrodialysis, Environ. Sci. Technol. **54**, 527 (2020).

[26] H. Tian, M. A. Alkhadra, K. M. Conforti, and M. Z. Bazant, Continuous and selective removal of lead from drinking water by shock electrodialysis, ACS ES&T Water **1**, 2269 (2021).

[27] K. M. Conforti and M. Z. Bazant, Continuous ion–selective separations by shock electrodialysis, AIChE J. **66**, e16751 (2020).

[28] M. B. Andersen, M. van Soestbergen, A. Mani, H. Bruus, P. M. Biesheuvel, and M. Z. Bazant, Current-induced membrane discharge, Phys. Rev. Lett. **109**, 108301 (2012).

[29] V. V. Nikonenko, A. V. Kovalenko, M. K. Urtenov, N. D. Pismenskaya, J. Han, P. Sistat, and G. Pourcelly, Desalination at overlimiting currents: State-of-the-art and perspectives, Desalination **342**, 85 (2014).

[30] E. Kniaginicheva, N. Pismenskaya, S. Melnikov, E. Belashova, P. Sistat, M. Cretin, and V. Nikonenko, Water splitting at an anion-exchange membrane as studied by impedance spectroscopy, J. Membr. Sci. **496**, 78 (2015).

[31] A. Yaroshchuk, E. Zholkovskiy, S. Pogodin, and V. Baulin, Coupled concentration polarization and electroosmotic circulation near micro/nanointerfaces: Taylor–Aris model of hydrodynamic dispersion and limits of its applicability, Langmuir **27**, 11710 (2011).

[32] I. Rubinstein and B. Zaltzman, Convective diffusive mixing in concentration polarization: From Taylor dispersion to surface convection, J. Fluid Mech. **728**, 239 (2013).

[33] E. V. Dydek and M. Z. Bazant, Nonlinear dynamics of ion concentration polarization in porous media: The leaky membrane model, AIChE J. **59**, 3539 (2013).

[34] T. A. Zangle, A. Mani, and J. G. Santiago, On the propagation of concentration polarization from microchannel-nanochannel interfaces. Part II: Numerical and experimental study, Langmuir **25**, 3909 (2009).

[35] A. Mani, T. A. Zangle, and J. G. Santiago, On the propagation of concentration polarization from microchannel-nanochannel interfaces. Part I: Analytical model and characteristic analysis, Langmuir **25**, 3898 (2009).

[36] E. V. Dydek, B. Zaltzman, I. Rubinstein, D. S. Deng, A. Mani, and M. Z. Bazant, Overlimiting current in a microchannel, Phys. Rev. Lett. **107**, 118301 (2011).

[37] A. Yaroshchuk, Over-limiting currents and deionization "shocks" in current-induced polarization: Local-equilibrium analysis, Adv. Colloid Interface Sci. **183-184**, 68 (2012).

[38] S. Schlumpberger, R. B. Smith, H. Tian, A. Mani, and M. Z. Bazant, Deionization shocks in crossflow, AIChE J. **67**, e17274 (2021).

[39] H. Tian, M. A. Alkhadra, and M. Z. Bazant, Theory of shock electrodialysis I: Water dissociation and electroosmotic vortices, J. Colloid Interface Sci. **589**, 605 (2021).

[40] S. Alizadeh, M. Z. Bazant, and A. Mani, Impact of network heterogeneity on electrokinetic transport in porous media, J. Colloid Interface Sci. **553**, 451 (2019).

[41] S. Alizadeh and A. Mani, Multiscale model for electrokinetic transport in networks of pores, Part II: Computational algorithms and applications, Langmuir **33**, 6220 (2017).

[42] S. Alizadeh and A. Mani, Multiscale model for electrokinetic transport in networks of pores, Part I: Model derivation, Langmuir **33**, 6205 (2017).

[43] M. Mirzadeh, T. Zhou, M. A. Amooie, D. Fraggedakis, T. R. Ferguson, and M. Z. Bazant, Vortices of electro-osmotic flow in heterogeneous porous media, Phys. Rev. Fluids **5**, 103701 (2020).

[44] M. A. Alkhadra, M. L. Jordan, H. Tian, C. G. Arges, and M. Z. Bazant, Selective and chemical-free removal of toxic heavy metal cations from water using shock ion extraction, Environ. Sci. Technol. **56**, 14091 (2022).

[45] H. B. Ulusoy Erol, C. N. Hestekin, and J. A. Hestekin, Effects of resin chemistries on the selective removal of industrially relevant metal ions using wafer-enhanced electrodeionization, Membranes **11**, 45 (2021).

[46] V. M. Palakkal, L. Valentino, Q. Lei, S. Kole, Y. J. Lin, and C. G. Arges, Advancing electrodeionization with conductive ionomer binders that immobilize ion-exchange resin particles into porous wafer substrates, npj Clean Water **3**, 5 (2020).

[47] H. Tian, M. A. Alkhadra, and M. Z. Bazant, Theory of shock electrodialysis II: Mechanisms of selective ion removal, J. Colloid Interface Sci. **589**, 616 (2021).

[48] D. A. G. Bruggeman, Berechnung verschiedener physikalischer konstanten von heterogenen substanzen. I. Dielektrizitätskonstanten und leitfähigkeiten der mischkörper aus isotropen substanzen, Ann. Phys. **416**, 636 (1935).

[49] R. B. Smith and M. Z. Bazant, Multiphase porous electrode theory, J. Electrochem. Soc. **164**, E3291 (2017).

[50] R. Dhopeshwarkar, R. M. Crooks, D. Hlushkou, and U. Tallarek, Transient effects on microchannel electrokinetic filtering with an ion-permselective membrane, Anal. Chem. **80**, 1039 (2008).

[51] I. Cohen and P. Kundu, *Fluid Mechanics* (Elsevier Science & Technology Books, San Diego, CA, 2008).

[52] J. N. Israelachvili, *Intermolecular and Surface Forces*, 3rd ed. (Academic, Burlington, MA, 2011).

[53] R. P. Misra, J. P. de Souza, D. Blankschtein, and M. Z. Bazant, Theory of surface forces in multivalent electrolytes, Langmuir **35**, 11550 (2019).

[54] J. P. de Souza and M. Z. Bazant, Continuum theory of electrostatic correlations at charged surfaces, J. Phys. Chem. C **124**, 11414 (2020).

[55] S. H. Behrens and D. G. Grier, The charge of glass and silica surfaces, J. Chem. Phys. **115**, 6716 (2001).

[56] F. H. J. van der Heyden, D. Stein, and C. Dekker, Streaming currents in a single nanofluidic channel, Phys. Rev. Lett. **95**, 116104 (2005).

[57] M. Shinozuka and C.-M. Jan, Digital simulation of random processes and its applications, J. Sound Vib. **25**, 111 (1972).

[58] M. Shinozuka and G. Deodatis, Simulation of stochastic processes by spectral representation, Appl. Mech. Rev. **44**, 191 (1991).

[59] See Supplemental Material at http://link.aps.org/supplemental/10.1103/PhysRevFluids.9.073701 for additional illustrations of the porous structures, simulation results, and videos of the simulations.

[60] G. Carta and A. Jungbauer, *Protein Chromatography: Process Development and Scale-Up* (Wiley-VCH, Weinheim, 2010).

[61] C. L. Druzgalski, M. B. Andersen, and A. Mani, Direct numerical simulation of electroconvective instability and hydrodynamic chaos near an ion-selective surface, Phys. Fluids **25**, 110804 (2013).